Part III

TOWARDS THE INDUSTRIAL GEOMETRY

9

TUBE WITH MIXING VANES : DEBORA-PROMOTEUR AND AGATE-PROMOTEUR EXPERIMENTS

Contents

9.1 Introduction **145**
9.2 DEBORA-Promoteur **145**
9.2.1 Test Section and Experimental Campaigns 145
9.3 AGATE-Promoteur **147**
9.4 Analysis of the DEBORA-Promoteur Experimental Measurements **148**
9.4.1 Estimation of the Bubble Diameter 150
9.5 Conclusions **152**

9.1 INTRODUCTION

In PWR cores, the industrial geometry is tremendously complex compared to traditional experimental setup usually consisting of simple tubes such as in the DEBORA experiment (Chapter 2). Although simple geometries are absolutely mandatory for verification and validation of the multi-scale physics modeling involved in boiling two-phase flows, it would hardly suffice to be perform a full scaling of the industrial configurations.

To that extent, there is a need for experimental measurements both in representative flow conditions **and** geometry. This implies reproducing test sections including complicated shapes such as grids inducing significant transverse flow and turbulent mixing.

In this Chapter, we focus on such a dedicated experiment called DEBORA-Promoteur and propose some analyses of its experimental measurements. Its single-phase counterpart called AGATE-Promoteur is also presented.

9.2 DEBORA-PROMOTEUR

9.2.1 *Test Section and Experimental Campaigns*

In 2003, the wish to investigate boiling flows in complex geometries similar to those of PWR fuel assembly motivated CEA and EDF to perform modifications of the DEBORA facility [35]. In order to mimic the turbulent mixing induced by the grids holding the fuel rods, a mixing device equipped with blades was built with respect to the geometrical properties of the mixing vanes of the PWR grids (Figure 9.1).

This mixing device was then welded into the DEBORA test section, thus named DEBORA-Promoteur. Its position upstream the end of the heating length was meant to induce a strong rotation in the flow in order to quantify the impact of the mixing regarding:

- Bubble recondensation for subcooled boiling ;
- Void redistribution for saturated cases ;
- Critical Heat Flux value compared to the naked pipe case.

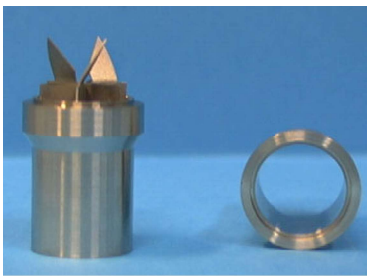

Figure 9.1: Picture of the mixing device. (Adapted from [34])

Figures 9.2a and 9.2b present the position of the measurement radius along with a sketch of the experiment, defining the position of the mixing vanes (MV) upstream the measurements section at a distance L_{MV}.

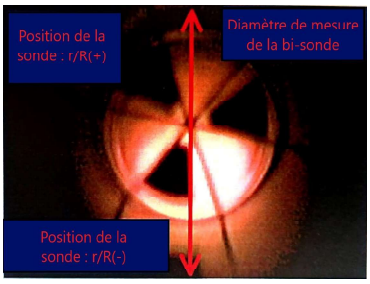

(a) Measurement radius. (Adapted from [35])

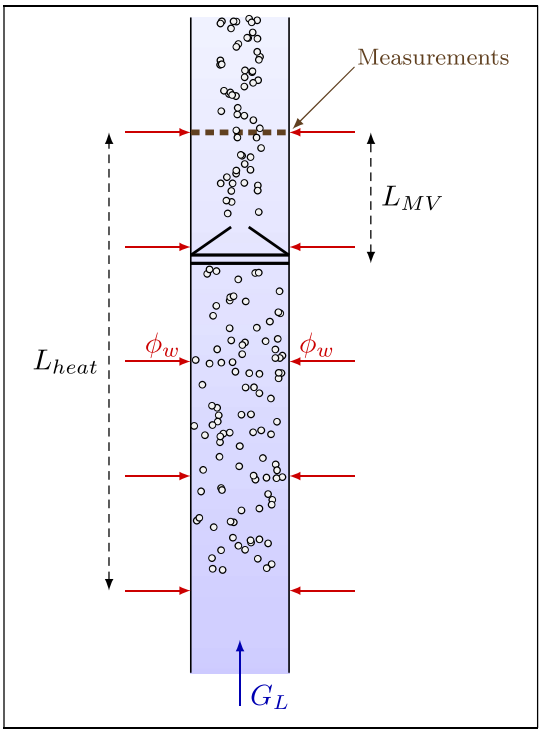

(b) Sketch of the DEBORA-Promoteur test section.

Figure 9.2: Description of the DEBORA-Promoteur experiment.

The same measurement instrumentation as the DEBORA C3000 cases (bi-optical probe, Figure 2.6) was used to study the flow topology in the DEBORA-Promoteur experiment. In that regard, two measurements campaign were conducted:

- Campaign C4800 where the mixing vanes were placed at $L_{MV} = 23.5\ D_h$ (≈ 0.45 m)upstream the end of the heating length [35] ;

- Campaign C5200, where the mixing vanes were placed $L_{MV} = 10\ D_h$ (≈ 0.19 m) upstream the end of the heating length [36].

Note : Unfortunately, no thermal measurement campaign was conducted on the DEBORA-Promoteur facility.

The different cases of the DEBORA-Promoteur experiment follow the same nomenclature as the DEBORA ones (Section 2.4). A total of three test series were conducted: 48G3P26W23, 52G3P26W23 and 52G3P26W27.

1. Series 48G3P26W23 ;
2. Series 52G3P26W23 ;
3. Series 52G3P26W27.

Regarding the available data for each test, bi-optical probes allow the measurements of the void fraction but also bubble diameter using the vapor (or interfacial) velocity as explained in Subsection 2.3.2. However, the measurement of the vapor velocity if:

1) The flow is mainly one-directional and aligned with the probles ;
2) Vapor phase is composed of spherical bubbles ;
3) Velocity gradient and center density gradient are small along a distance equal to the bubble diameter.

Since the mixing vanes introduce a strong mixing and rotational effect, hypothesis 1) is, at first glance, impossible to verify and ensure that measurements of vapor velocity are correct. For each dataset, the available experimental file contains:

- 48G3P26W23: Void fraction α and interference frequency ν value for each probe (1 and 2)
- 52G3P26W23 & 52G3P26W27: void fraction α and interference frequency ν value for each probe (1 and 2) plus the estimated (potentially uncertain) vapor velocity $U_{V,z}$.

9.3 AGATE-PROMOTEUR

Following the DEBORA-Promoteur tests, experimental findings lead CEA and EDF to investigate the single-phase liquid velocity profile in the mixing vanes geometry. This lead to the development of an experiment called AGATE-Promoteur.

The AGATE-Promoteur experiments consist of LDV (Laser Doppler Velocimetry) measurements of the liquid velocity and turbulent intensity in both axial and radial direction. The test in conducted using the very same geometry and mixing vanes as the DEBORA-Promoteur case and consists of a single set of measurements for water at 2 bar flowing at a mass flow rate $G_L \approx 3000$ kg/m^2/s (same mass flux as the DEBORA-Promoteur cases) and $T_L \approx 40$°C, resulting in an hydraulic Reynolds number $\mathrm{Re}_{D_h} \approx 8.5 \times 10^4$. Measurements are then operated at several axial positions (18) and diameters (6). Figure 9.3 details the different positions where measurements were conducted.

Each diameter has 24 points of measurements, with a total of 108 diameters covered in the whole test both upstream and downstream of the mixing vanes.

For each data point, we have the local axial velocity, radial velocity (signed positive or negative depending on its direction relative to the measured diameter), axial and radial turbulent intensities. Later, we will prefer reconstructing the values of the local RMS (Root Mean Square) of the velocity:

$$RMS_i := \sqrt{\langle U_i' U_i' \rangle} = I_{T,i} \times \langle U_i \rangle \tag{9.1}$$

where $i = A,\ R$ for axial or radial direction, $U = \langle U \rangle + U'$ the velocity decomposed between time-average and fluctuation, and I_T the measured turbulent intensity.

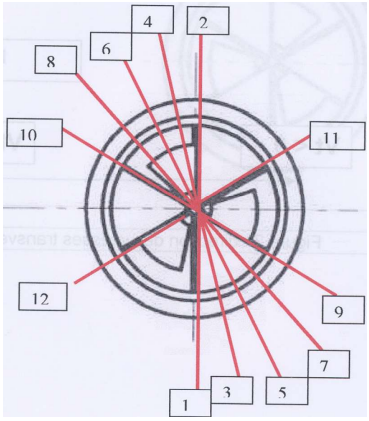

(a) Radial measurements diameters. (Adapted from [34])

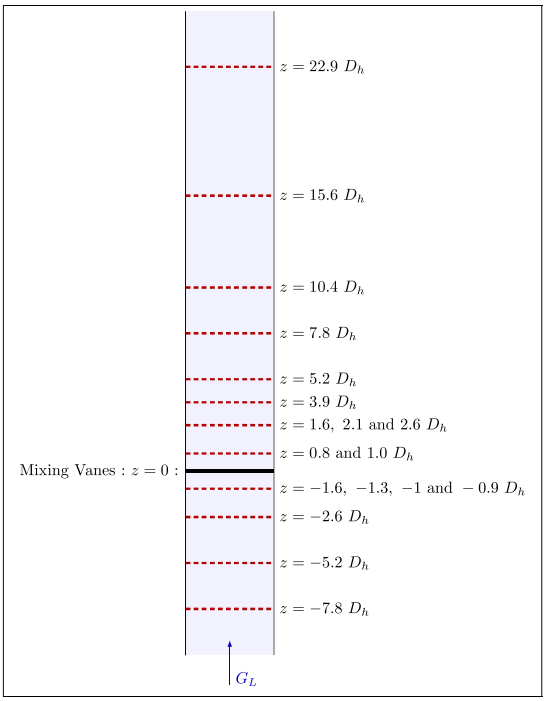

(b) Axial positions of measurements.

Figure 9.3: Covered measurements positions in AGATE-Promoteur experiment.

9.4 ANALYSIS OF THE DEBORA-PROMOTEUR EXPERIMENTAL MEASUREMENTS

On Figures 9.4, 9.5 and 9.6, we plot respectively the void fraction and interference frequency (averaged for the two probes) for campaigns 48G3P26W23, 52G3P26W23 and 52G3P26W27.

9.4.0.1 *48G3P26W23 cases*

The first immediate observation is the position of the void fraction peak positioned at the center of the tube (Figure 9.4a), strongly differing from the naked tube (Figure 2.7a). This is a direct consequence of the mixing vanes inducing a rotational flow that will gather the vapor at the center. Except for lowest quality cases, the void fraction at the wall is the minimum value along the measurement radius, which insists on the inversion of the void fraction profile under the mixing vanes effect.
Moreover, the profile is not perfectly symmetrical with a void peak progressively shifting towards positive values of r/R. This could be expected since the mixing vanes do not present any axisymmetry.

Analyzing the interference frequency (Figure 9.4b), *i. e.* the number of interface detection per second, allow to qualitatively determine whether if the measured void fraction at a given point is the result of

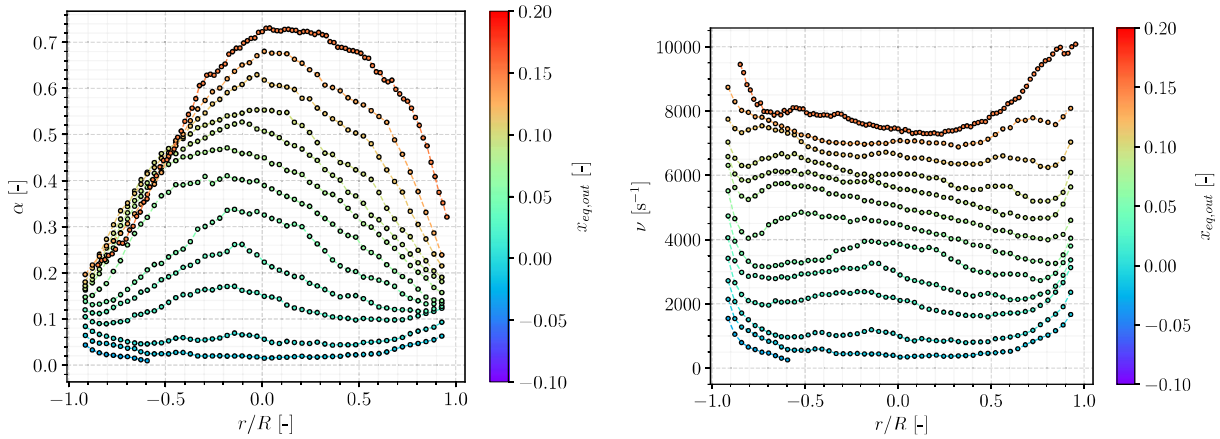

(a) Void fraction (b) Interference frequency

Figure 9.4: Experimental results from the 48G3P26W23 series.

a large number of small bubbles or a small number of large bubbles going through the probes. We note for hottest cases that the interference frequency reaches its maximum at the wall where the void fraction is the lowest, while its minimum is at the center where void fraction is maximal. This means that fewer bubbles at the center lead to a larger void fraction compared to the wall, which is likely to indicate the effect of coalescence increasing the average bubble size.

9.4.0.2 *52G3P26W23 and W27 cases*

The main difference between the C5200 and C4800 cases is the position of the mixing vanes that are closer to the end of the mixing length in the C5200 campaigns (10 D_h versus 23.5 D_h.

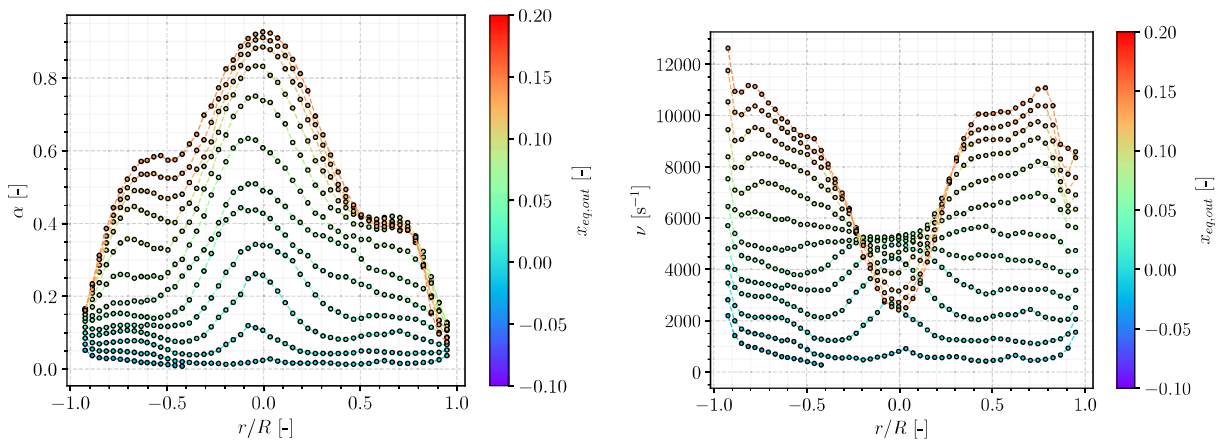

(a) Void fraction (b) Interference frequency

Figure 9.5: Experimental results from the 52G3P26W23 series.

Similar to C4800 cases, we observe a void fraction peak at the center and minimum at the wall (Figures 9.5a and 9.6a). However, the shape of the measurements largely differs by presenting local maximum values around $r/R = \pm 0.6$ for hottest cases. The void fraction peaks are also higher than for C4800 cases, with values up to 90%. This is probably an effect of the MV positions since moving the vanes downwards means that the flow will be mixed later, leaving a shorter distance for the flow to fall back to a traditional single tube profile. The amount of vapor suddenly brought to the center will increase as the distance between the vanes and the measurement section reduces.

Remark : Such an effect may be assimilated to a so-called "history effect", meaning that the distance to such a mixing device has an impact over the two-phase flow properties.

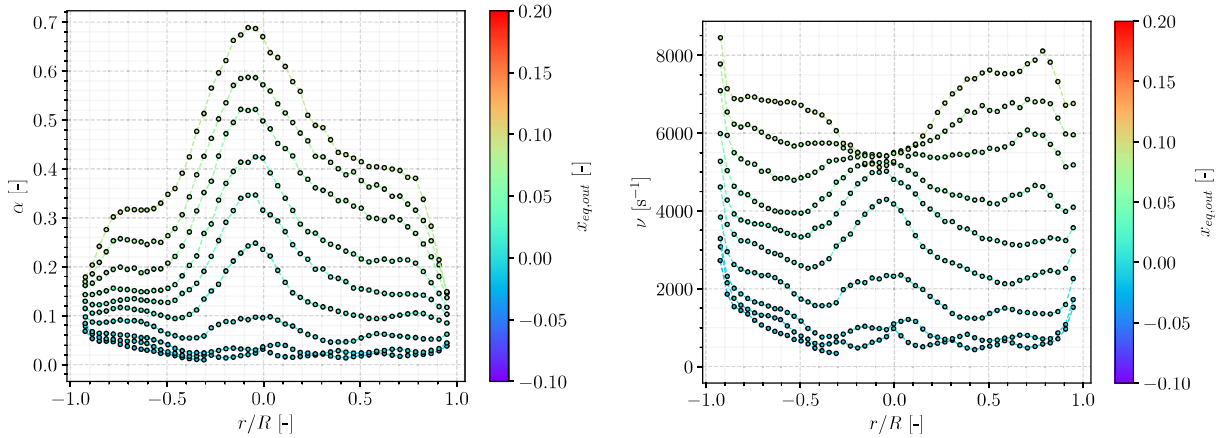

(a) Void fraction

(b) Interference frequency

Figure 9.6: Experimental results from the 52G3P26W27 series.

Interference frequencies (Figures 9.5b and 9.6b) profiles are also differing from C4800 cases. The interference peak is initially located at the center for low quality cases, meaning that there is a larger number of bubbles at the center compared to the wall. However, the shape reverses as the outlet quality increases (and thus the core void fraction), with a huge decrease of the bulk interference frequency which significantly points towards predominant coalescence effects. Noting that this change happens roughly when $x_{eq,out} \leq 0$ (saturation is reached) indicates that it may originates from the absence of condensation.

Remark : The considerations over condensation are though speculative and would largely benefit from liquid temperature measurements in such a configuration, which could both quantify the impact of mixing on the liquid phase and correlate interference frequencies to local subcooling values.

9.4.1 *Estimation of the Bubble Diameter*

Since values of vapor velocity measurements are given for the C5200 cases, one may be interested in exploiting them to try to extract information about the bubble size distribution in the flow. However, we have to be able to tell whether those measurements were largely erroneous due to the rotation effects or not *i. e.* if the bubbles were moving in the direction of the probes.

To do so, we propose two arguments:

- Analyzing the difference between the measured interference frequencies for each probe, which could help to quantify if the number of bubbles detected largely differ between them. If so, it means a strong rotation made bubbles flowing through only one probes. On the contrary, this would support the fact that, locally, bubbles were globally flowing in the direction of the probes.
- Quantifying the importance of the radial velocity compared to the axial velocity in the measurement section.

On Figure 9.7, we plot the relative difference of interference frequency between the two probes for each C5200 campaign.

We see that, close to the wall, the interface detection of the probes differ by up to 35%, which clearly indicates a vapor phase moving radially. However, as we approach the center ($-0.75 \leq r/R \leq 0.75$), the difference in interference frequency globally falls below 5%, potentially showing that bubbles at those locations were having mostly axial velocities.

To quantify the importance of the radial velocity at the measurement section ($z \approx 10\ D_h$ after the grids), we rely on the AGATE-Promoteur experimental results (Section 9.3). Based on the different measured diameters at each axial position, we can compute the average value of the ratio between radial and axial velocities U_R/U_A depending on the height z. The results are shown on Figure 9.8

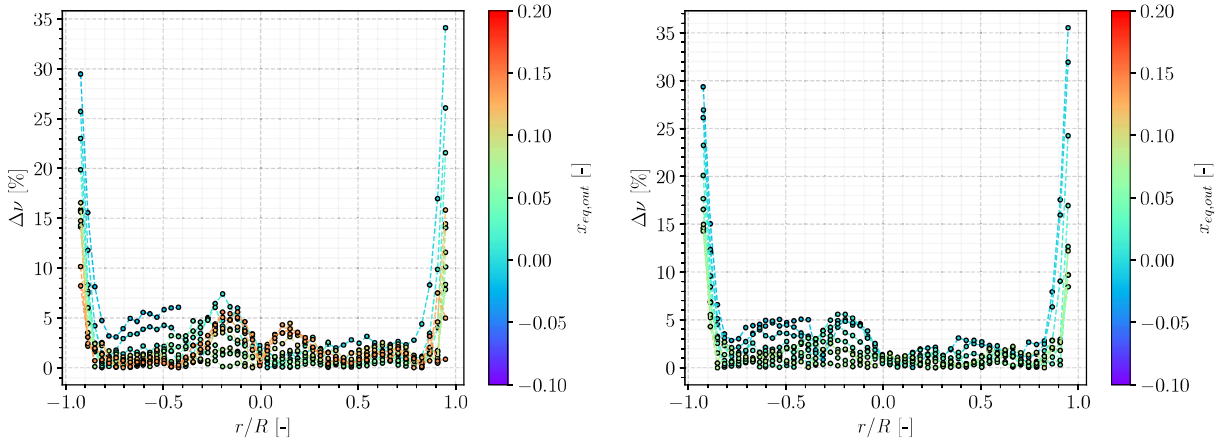

(a) 52G3P26W23 series

(b) 52G3P26W27 series

Figure 9.7: Relative difference of interference frequency for the two probes.

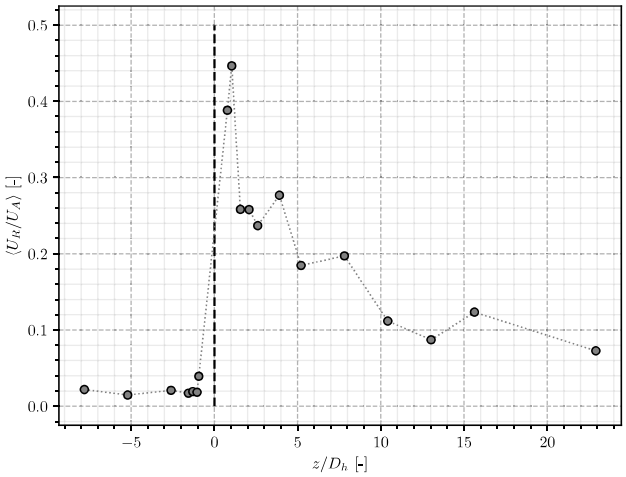

Figure 9.8: Average relative importance of radial velocity to axial velocity in AGATE-Promoteur experiment. Black dotted lines denotes the position of the MV.

The mixing effect on liquid velocity is clear: the average induced rotation velocity can reach up to 45% of the axial velocity in the section right after the MV. The importance of the radial velocity then naturally fades with the distance to the MV, becoming of the order of 10% at $z \approx 10\ D_h$.

At the position corresponding to the measurements in the C5200 campaign, the radial velocity then is approximately 10 times smaller than the axial velocity. This comforts the fact that the flow direction is mainly radial when the measurement using the bi-optical probe is conducted.

Altogether, those two analyses both support the fact that the hypothesis of a flow aligned with the probes at $z = 10\ D_h$ downstream the MV is reasonable. Therefore, we allow ourselves to use the measured values of the vapor velocity $U_{V,z}$ **between** $r/R = -0.75$ **and** $r/R = 0.75$ in the C5200 cases to propose **an estimation** of the bubble diameter in DEBORA-Promoteur measurements:

$$D_V \approx \frac{6\alpha U_{v,z}}{4\nu} \tag{9.2}$$

Resulting values are presented on Figure 9.9.

First, we notice that the values attained closer to the wall mostly lie between 0.1 mm and 0.5 mm which is coherent with the values observed in the naked tube case (Figure 2.7c).

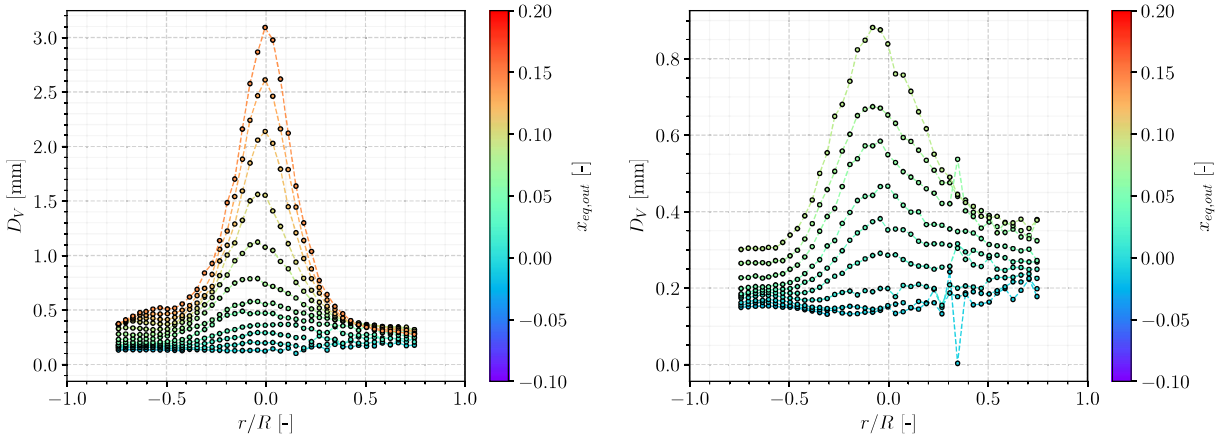

(a) 52G3P26W23 series

(b) 52G3P26W27 series

Figure 9.9: Estimation of bubble diameter on C5200 measurements series.

When approaching the center of the pipe for high qualty cases, the bubble diameter sharply increase with values that can reach up to 3 mm. In those conditions, such a diameter is the result of an important coalescence along with negligible condensation effects. Although very large void fractions are reached, those bubble diameters are still an order of magnitude lower than the tube diameter meaning we are not in presence of a slug or annular flow at the center. The resulting flow regime at high void fractions is likely look like a foam composed of several millimeter bubbles separated by thin layers of liquid.

Remark : In such two-phase flow conditions, the dispersed approach is unlikely to be representative of the real physics at stake. Strong interaction between the bubbles can be expected and the nearly absence of liquid means it can not be considered as the leading fluid anymore.

Moreover, the optimal packing for non-overlapping spheres of same sizes is mathematically capped at 74% [133], bubbles at void fraction $\alpha > 74\%$ then must have, at least partially, non-spherical shapes. Which is also supported by Weber number value We ~ 0.1 and Eötvös value Eo ~ 1 in those conditions.

9.5 CONCLUSIONS

The analysis of the DEBORA-Promoteur experiment allowed to qualitatively qualify the two-phase flow in a geometry including mixing vanes. So far, we can remember that:

- The mixing vanes have a clear impact on the vapor distribution, gathering it at the center of the tube thus reversing the radial void fraction profile.
- The axial distance to the mixing vanes appears to have a significant influence over the vapor distribution, further enlightening the presence of a "history effect".
- An estimation of the bubble diameter in those conditions was achievable and showed very important coalescence effects with bubble diameters increasing up to 10 times larger when moving from the wall to the center.
- Void fraction can reach very high values with peaks at the center up to 90%, which combined with the bubble diameter value indicates that the flow may look like a foam composed of vapor bubbles with thin layers of liquid between them.

In the next chapter, we perform numerical simulations of the DEBORA-Promoteur and AGATE-Promoteur experiments to assess NEPTUNE_CFD capacity on such geometries.

10

NEPTUNE_CFD SIMULATIONS OF DEBORA-PROMOTEUR AND AGATE-PROMOTEUR CASES

Contents

10.1 NEPTUNE_CFD simulations of DEBORA-Promoteur cases **153**
10.1.1 Simulation Setup 153
10.1.2 Results 154
10.2 NEPTUNE_CFD simulations of AGATE-Promoteur cases **156**
10.2.1 Simulation Setup 156
10.2.2 Results 157
10.3 Conclusions **160**

In this Chapter, we conduct NEPTUNE_CFD simulations of the DEBORA-Promoteur and AGATE-Promoteur experiments. The results are presented as a prospective study of the capacity of the code to handle complex geometries approaching the industrial configuration.

10.1 NEPTUNE_CFD SIMULATIONS OF DEBORA-PROMOTEUR CASES

10.1.1 *Simulation Setup*

Contrary to the DEBORA simulations (Chapter 3), the physics involved in the DEBORA-Promoteur case are intrinsically three-dimensional and can therefore not be reduce the problem to 2D-axisymmetric computations. The computational domain is thus a 4m long vertical tube of radius $R = 9.6$ mm, with base of the mixing blades positioned at the axial height $z = 0$. The heated section is translated axially to adapt the simulation for each position of the mixing vanes (23.5 D_h for C4800 and 10 D_h for C5200), giving the following boundary conditions:

- Uniform wall heat flux for -3.055 m $\leq z \leq 0.445$ m (C4800) or -3.318 m $\leq z \leq 0.182$ m (C5200) ;
- Adiabatic wall for remaning wall faces ;
- Uniform outlet pressure ;
- Uniform liquid inlet velocity and temperature.

A mesh sensitivity conducted to use the mesh presented on Figure 10.1 which contains a total of 3 487 267 cells.

We simulated 3 cases per series 48G3P26W23 and 52G3P26W23, covering the two MV positions and different outlet quality ($x_{eq,out}$) :

- 48G3P26W23Te65 & 52G3P26W23Te65 with $x_{eq,out} \approx 0\%$
- 48G3P26W23Te69 & 52G3P26W23Te69 with $x_{eq,out} \approx 5\%$
- 48G3P26W23Te75 & 52G3P26W23Te75 with $x_{eq,out} \approx 12.5\%$

Note : The computational times was ensured to be long enough to reach time-average convergence of the simulations.

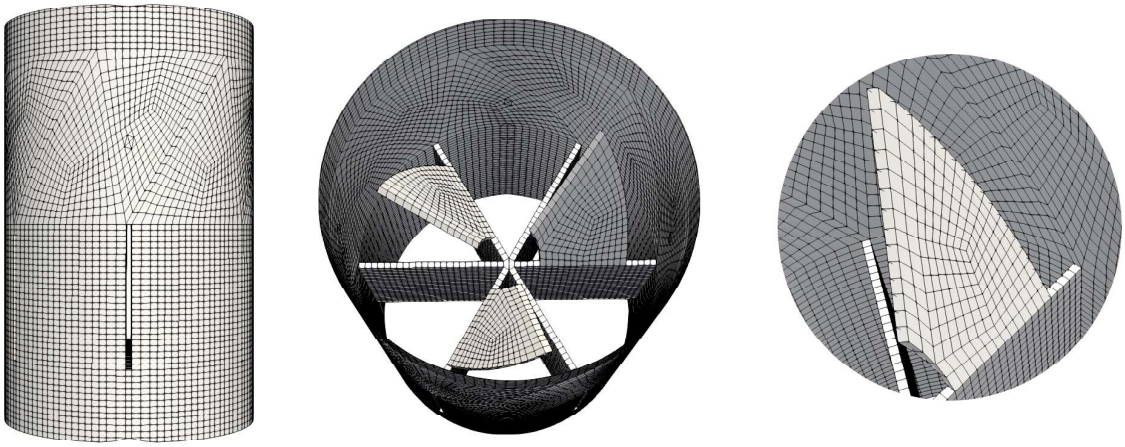

Figure 10.1: Meshing of the mixing vanes region.

Results are compared to the experimental measurements *i. e.* only void fraction for C4800 cases and void fraction, bubble diameter and vapor velocity for C5200 cases.

Remark : Following the discussions regarding vapor velocity and bubble diameter estimation for C5200 cases (Chapter 9), comparison with the CFD results will rather be of qualitative nature since we can't ensure the accuracy of the measurements.

10.1.2 *Results*

Results are presented on Figure 10.2.

Quantitatively speaking, it seems that NEPTUNE_CFD reproduces the effect of vapor acculumation at the center under the pressure gradient generated by the swirl induced by the mixing vanes. The radial position of the core void fraction peak correctly matches the experimental one. The Te65 cases (Figure 10.2a) are reasonably predicted with void fractions values at the center close to the measurements, with the C5200 simulation much closer to the experimental profile. However, Te69 and Te75 cases (Figures 10.2b and 10.2c) are showing much larger discrepancies with the experiments. The core void fraction peak appears largely overestimated for $T_{L,in} = 69°\text{C}$ with $\alpha\,(r/R = 0) \approx 70\%$ and do not change when moving to $T_{L,in} = 75°\text{C}$ where the void fraction profile rather flattens. Such a behavior strongly differs form the experiments where a large increase in core void fraction when inlet temperature increases. Moreover, the particular shape of 52G3P26W23Te75 case where local maximum for α are observed at $r/R \approx \pm 0.6$.

Remark : The computed void fraction seems unable to go above 70% in this case, which is in contradiction with the experiments. However, a sensitivity test showed that removing the added mass force (Eq. 1.24) from the interfacial momentum transfer allowed the bulk void fraction to reach 90%.

Regarding C5200 cases, bubble diameter profiles appear coherent with the experimental estimations for Te65 and Te69 cases (Figure 10.2d and 10.2e). In particular, the growth towards the center due to coalescence is fairly reproduced in Te69 case. On the contrary, the very large estimated values for Te75 case ($D_V \sim 2$ mm) are completely missed by the simulation (Figure 10.2f).

Remark : As discussed in the analysis of the experimental results (Subsection 9.4.1), the flow regime encountered in the 52G3P26W3Te75 case is very likely deviate from a dispersed bubbly flow, explaining the inability of the simulations to reproduce this behavior.

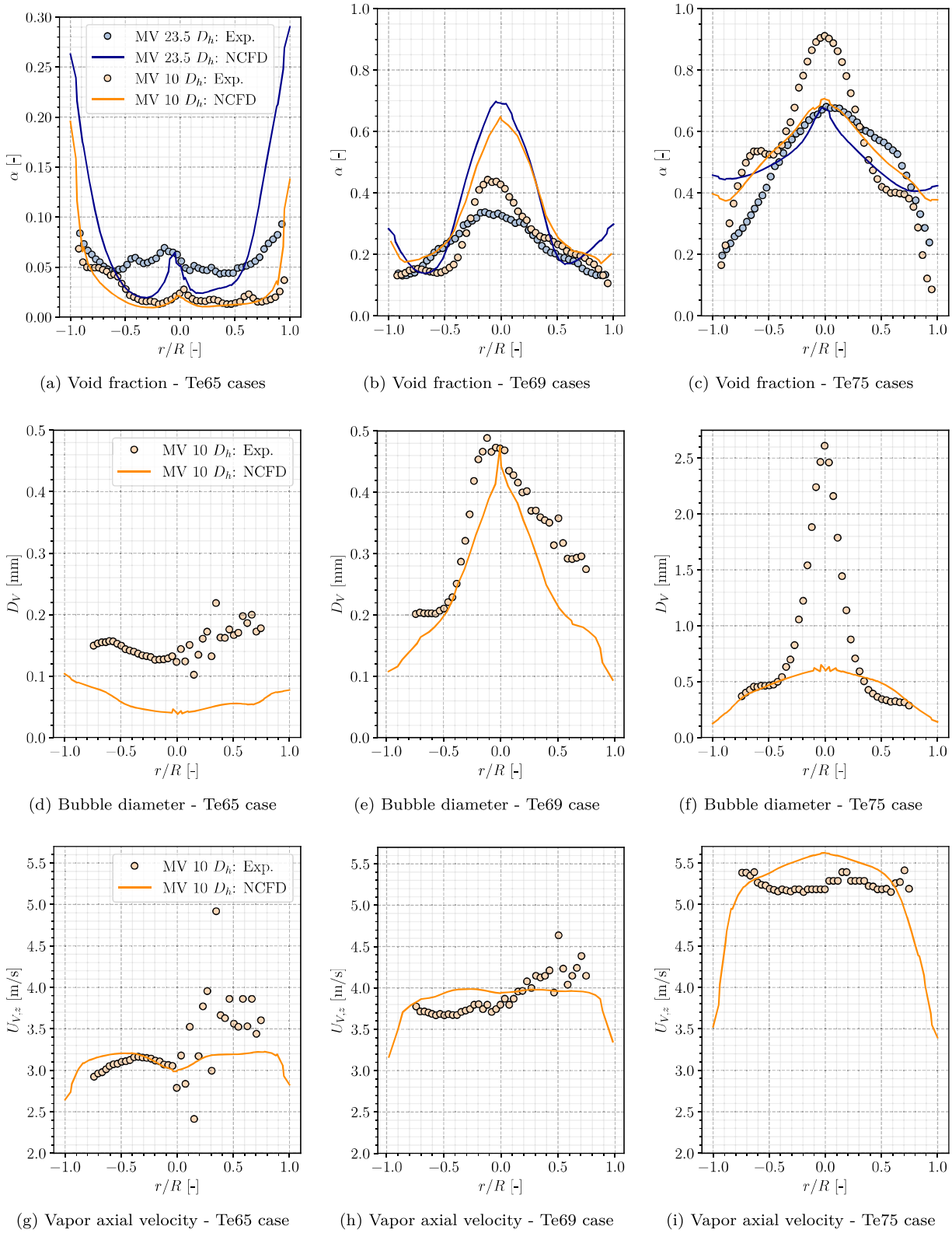

(a) Void fraction - Te65 cases (b) Void fraction - Te69 cases (c) Void fraction - Te75 cases

(d) Bubble diameter - Te65 case (e) Bubble diameter - Te69 case (f) Bubble diameter - Te75 case

(g) Vapor axial velocity - Te65 case (h) Vapor axial velocity - Te69 case (i) Vapor axial velocity - Te75 case

Figure 10.2: NCFD results on the DEBORA-Promoteur cases. MV at 23.5 D_h and 10 $D_h$respectively correspond to C4800 and C5200 cases.

Finally, the order of magnitude of predicted vapor velocities increase with the inlet temperature (Figures 10.2g, 10.2h, 10.2i) similarly to the experimental estimations.

To further investigate the mixing vanes geometry and understand the large discrepancies on the void fraction profiles (Figures 10.2b and 10.2c), we perform simulations of the single-phase AGATE-Promoteur case in next Section.

10.2 NEPTUNE_CFD SIMULATIONS OF AGATE-PROMOTEUR CASES

10.2.1 *Simulation Setup*

Simulations of the AGATE-Promoteur case are done using *code_saturne* 7.0, the single-phase counterpart of NEPTUNE_CFD. The computational domain is 0.7 m long (shorter than DEBORA-Promoteur case since we don't need to apply the 3.5m heating) with the mixing blades positioned at $z = 0$. Using the same meshing used for the DEBORA-Promoteur cases (Figure 10.1), the total mesh contains 1 905 357 cells.

Two simulations are performed using the turbulence model $R_{ij} - \varepsilon$ SSG with a smooth wall two-scale turbulent law and with a rough wall turbulent law (average roughness $\epsilon = 10^{-5}$ m fixed arbitrarily as a sensitivity test) [147].

Note : Before comparisons with experiments, we made sure that NEPTUNE_CFD two-phase solver and *code_saturne* single-phase solver produced similar results when simulating a single-phase flow using the $R_{ij} - \varepsilon$ SSG model.

To test the sensitivity to turbulence modeling, we also realize a Large Eddy Simulation (LES) using the LES WALE (Wall-Adapting Local Eddy-Viscosity) model [147]. For this simulation, we use a more refined mesh (Figure 10.3) containing a total of 121 942 848 cells.

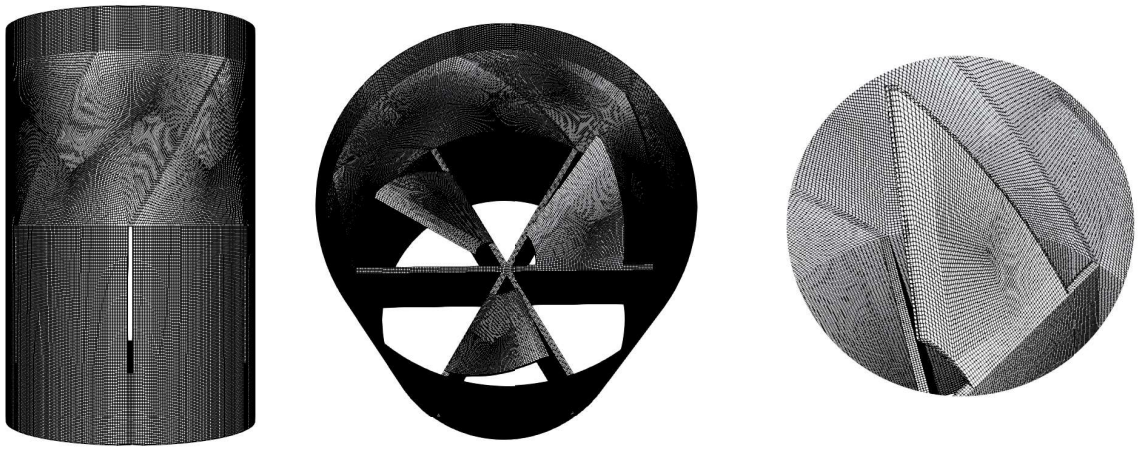

Figure 10.3: Mesh

In this configuration, we achieve an average wall distance $y^+ \approx 13$ in the whole domain, which is too large to numerically resolve the boundary layer meaning a wall-law will be used to evaluate the liquid velocity in the wall cell.

Note : : Astable time-convergence of all the variables is achieved for the LES computation after 10 s of simulated physical time.

Finally, we want to compare the results of the simulations with measurements of the RMS of the velocity fluctuations (Eq. 9.1), meaning that we have to reconstruct those values from the CFD computations. Since we perform Unsteady-RANS (URANS) simulations (using the $R_{ij} - \varepsilon$ SSG model), fluctuations of the velocity field are both modeled in the components of the Reynolds Stress Tensor and partly simulated

due to the potential time-oscillations of the average velocity field $\langle \overline{U} \rangle$. Therefore, the RMS for URANS simulations is computed using the modeled components of the Reynolds Stress Tensor $R_{ij,mod}$:

$$RMS_{A,URANS} = \sqrt{R_{zz,mod} + \langle (\tilde{U} \otimes \tilde{U})_{zz} \rangle} \tag{10.1}$$

where $\tilde{U} = \langle \overline{U} \rangle - \overline{U}$ is the instantaneous difference between the velocity field and its time average *i. e.* the simulated fluctuations of the URANS computation.

Regarding the LES computation, the fluctuations of the velocity field are mainly simulated and are thus only contained in the instantaneous velocity field $\overline{U}$. Therefore, they are computed as:

$$RMS_{A,LES} = \sqrt{\langle (\tilde{U} \otimes \tilde{U})_{zz} \rangle} \tag{10.2}$$

The same operation is conducted for the radial RMS, which involves the components xx, yy and xy.

10.2.2 *Results*

In this section, we discuss results obtained at three different heights : 0.8 D_h, 10 D_h and 23 D_h downstream the mixing vanes.

10.2.2.1 0.8 D_h *After the Mixing Vanes*

Figure 10.4 shows the results less than a hydraulic diameter after the mixing vanes.

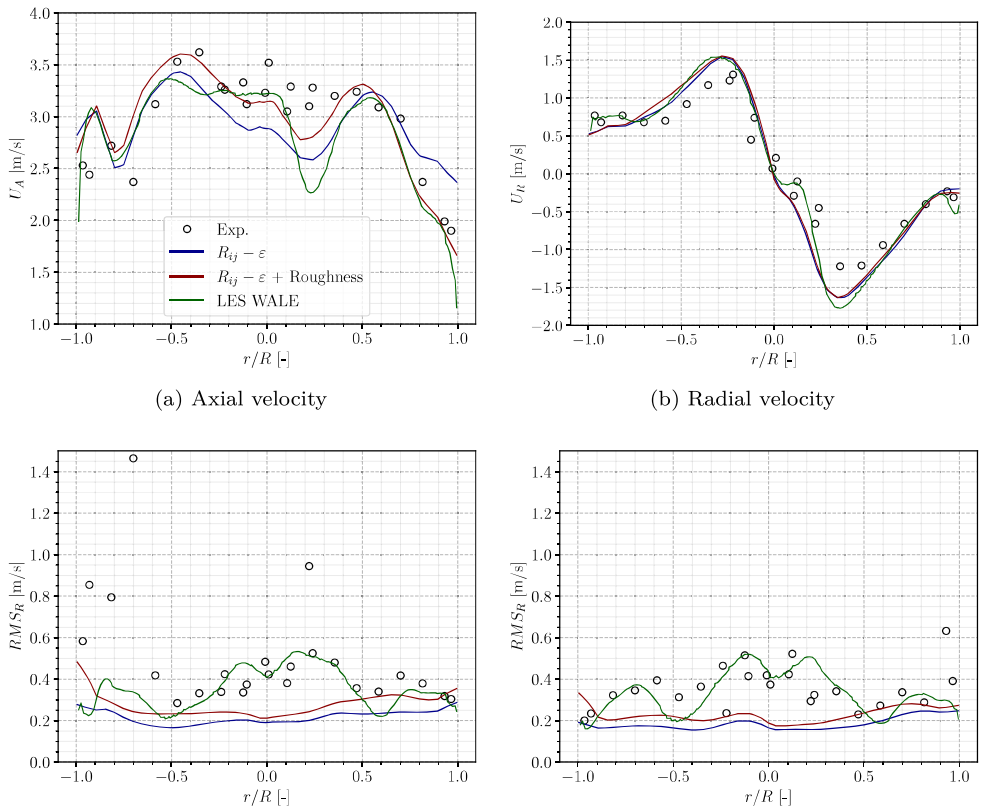

(a) Axial velocity

(b) Radial velocity

(c) Axial RMS

(d) Radial RMS

Figure 10.4: Results for $z = 0.8\ D_h$

The three simulations correctly match the experiments for the axial and radial velocities (Figures 10.4a and 10.4b). However, the velocity RMS (Figures 10.4c and 10.4d) are underestimated by the $R_{ij} - \varepsilon$ model, with the rough law use yielding slightly higher values. On the contrary, the LES simulation better reproduce the core velocity fluctuations especially near the center of the pipe.

10.2.2.2 10 D_h *After the Mixing Vanes*

Figure 10.5 shows the results at 10 D_h downstream the mixing vanes, which corresponds to the distance at which two-phase flow measurements of the DEBORA-Promoteur C5200 campaign was conducted (Section 9.2.

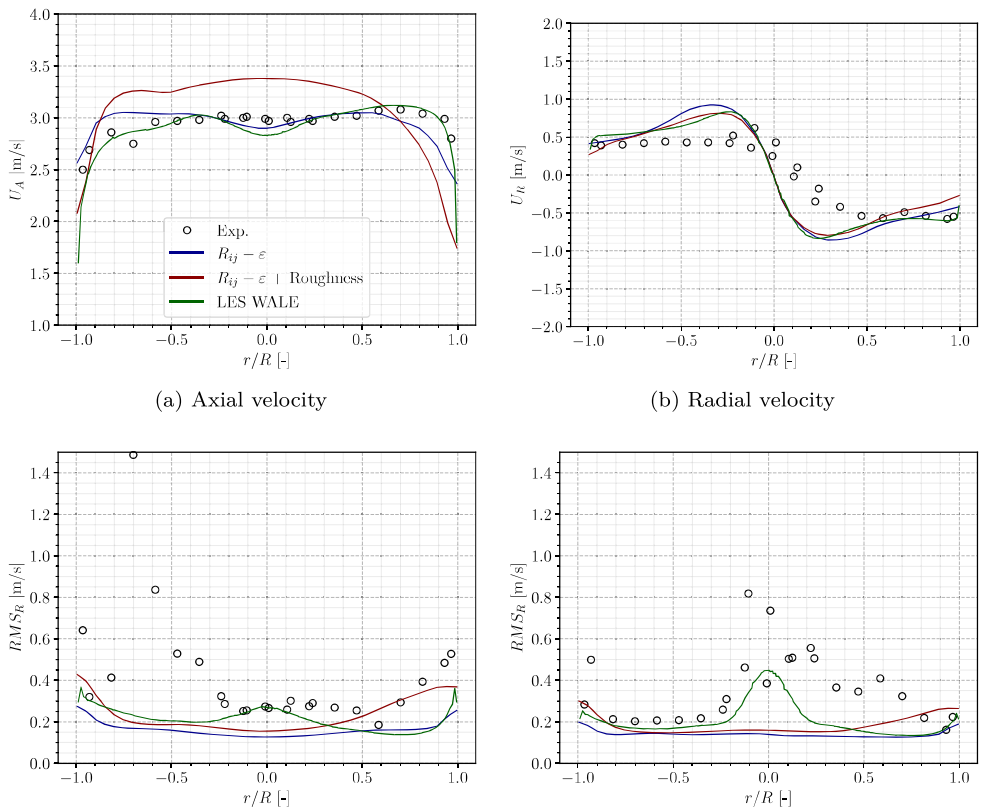

(a) Axial velocity

(b) Radial velocity

(c) Axial RMS

(d) Radial RMS

Figure 10.5: Results for $z = 10.4\ D_h$

Going further downstream, we observe that the use of the roughness law start to induce discrepancies on the axial velocity profile while the two other calculations still agree with the measurements (Figure 10.5a). Radial velocity is however equally predicted by the three simulations, with well reproduced wall values but all showing overestimation for $-0.5 \leq r/R \leq 0.5$ (Figure 10.5b), meaning that a too large bulk rotation of the fluid is predicted.

The velocity RMS are still better predicted by the LES computation (Figures 10.5c and 10.5d) but start to show underpredictions compared to the 1 D_h results. Close to the wall, the three modeling all perform similarly.

10.2.2.3 23 D_h *After the Mixing Vanes*

Finally, Figure 10.6 present results 23.5 D_h downstream the mixing vanes, which corresponds to the distance at which two-phase flow measurements of the DEBORA-Promoteur C4800 campaign was conducted (Section 9.2.

At this distance, the axial velocity profile has been significantly degraded by using the roughness law (Figure 10.6a) where the other modeling continue to match the measurements. However, the overestimation of the rotation velocity is amplified compared to the 10 D_h results for the smooth wall simulations while adding a roughness term seem to enhance the damping of the swirl induced by the vanes, better reproducing the experimental results (Figure 10.6b).

The axial velocity RMS are now better predicted by the rough wall simulation (Figure 10.6c) while the radial RMS is more accurately reproduced by the LES computation (Figure 10.6d).

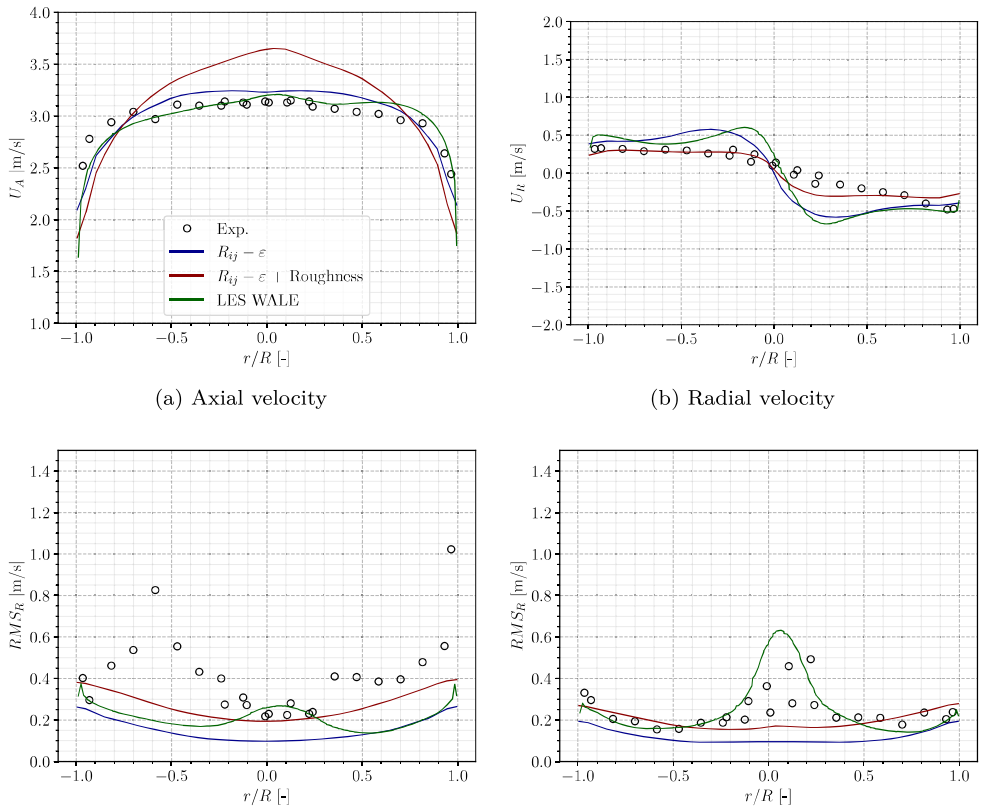

(a) Axial velocity

(b) Radial velocity

(c) Axial RMS

(d) Radial RMS

Figure 10.6: Results for $z = 22.9\ D_h$

10.2.2.4 *Interpretation Regarding the DEBORA-Promoteur Simulations*

Overall, the main characteristic of the single-phase simulation results on the AGATE-Promoteur case is the overestimation of the radial velocity when moving downstream the mixing vanes and reaching the axial positions corresponding to C4800 and C5200 measurements. In terms of hydrodynamics, it means the fluid's rotation is too large, which will result in a stronger pressure gradient between the wall and the center.

Transposing this result to a bubbly flow, the pressure gradient will be responsible for transverse migration of the bubbles towards the center of the pipe. If the rotation is overestimated, so will be the migration of bubbles which results in an excessive bubble accumulation in the core of the flow that should induce an overestimation of the local void fraction. This qualitative behavior is in agreement with the too large void fraction obtained in the simulations of DEBORA-Promoteur experiment (Figure 10.2).

Moreover, the discrepancy on the rotation increasing with the distance to the mixing vanes implies that boiling simulations would be more accurate for the C5200 cases than the C4800 cases (measurements 10 D_h downstream the MV versus. 23.5 D_h). That is actually true when looking at the void fraction profiles for Te65 and Te69 cases (Figures 10.2a and 10.2b) where larger differences with the measurements are observed for the C4800 simulations.

Remark : The main limitation of the presented single-phase simulations is the systematic use of a wall-law, which can have a strong impact regarding this geometry where the wall presence is ubiquitous in addition to the mixing vanes presence. A LES computation using an even finer meshing allowing to reach $y^+ \sim 1$ in the computational domain could bring insightful information to investigate the rotation overestimation.

10.3 CONCLUSIONS

In this Chapter, we performed CFD simulations on the tube equipped with mixing vanes geometry. Both boiling flow simulations using NEPTUNE_CFD and single-phase simulations with *code_saturne* were realized, respectively compared to DEBORA-Promoteur and AGATE-Promoteur experiments. So far, the main highlights of the results are:

- The boiling simulations of DEBORA-Promoteur cases showed reasonable qualitative behavior with bulk vapor accumulation, void fraction peak and bubble coalescence at the center, and vapor velocity increase with outlet quality.
- Yet, precise predictions of void fraction profiles could not be achieved with very large overestimation in the bulk plus the incapacity to reach void fractions higher than 70%. This could be associated to change in the multiphase flow regime that lie outside of the dispersed bubbly flow model capacity.
- Further investigations on the single phase case AGATE-Promoteur showed an excessive computed rotation of the fluid, increasingly differing from the experiments as we move downstream the mixing vanes. A too large swirl could explain the overestimation of the void fraction in the boiling case due to bubble transverse migration.
- Wall law seem to have a significant influence over the velocity profiles and may be an area of improvement, especially for confined geometries where solid walls are strongly influencing the flow.

Finally, we want to mention that achieving precise results for single-phase simulations on complex industrial geometries representative of PWR is still a very active field of research [75]. The use of RANS [5] or wall-modeled LES [41] approaches are still investigated in order to save computational time in the prospect of reaching simulations of a full fuel assembly by including, for instance, modeling of mixing vanes as source terms in the computational domain [14].